PFC/JA-86-26

Observations of Centrally Peaked Impurity Profiles Following Pellet Injection in the Alcator-C Tokamak

R. D. Petrasso, D. J. Sigmar, K. W. Wenzel, J. E. Hopf,

M. Greenwald, J. L. Terry and J. Parker[†]

1 May 1986

This is an extended version

of our document PFC/JA-85-41

(which was submitted to PRL in December 1985)

Plasma Fusion Center

Massachusetts Institute of Technology

Cambridge, Massachusetts 02139 USA

[†] present address: Varian Associates, Beverly, MA 01915

Abstract

Through the use of x-ray arrays, highly peaked carbon (C) and molybdenum (Mo) profiles were observed to occur after hydrogen pellet injection used for plasma fueling. Multi-ion neoclassical theory predicts equilibrium profiles close to these observations. Specifically, about 40 ms after pellet injection, C, a plateau impurity, was well fit by $(T_e/T_e(0))^{1.5Z_C}$ for $r \lesssim 6.5$ cm (Z_C=6). Experimental values for the convective velocity and diffusivity inside 4 cm were $\sim 10^3$ cm/s and ~ 300 cm^2/s, respectively. An internal disruption then occurred, which reduced on-axis impurities by a factor of 3 and ended neoclassical-like transport. Based on these observations we posit that C, the dominant non-hydrogenic contributor to Z_{eff}, dramatically affects sawtooth dynamics by altering the central resistivity. The implications of these observations to ignited plasmas are discussed.

The transport of impurities, and the ensuing implications for current profiles and sawtooth dynamics, are crucial issues for tokamak physics[1-4] and future reactor designs. Foremost, should alpha-particles behave neoclassically they could, in certain circumstances, accumulate in the center and quench the burn.[5] Despite significant work on neoclassical transport,[1-5] quantitative comparisons have been seriously impaired by the lack of complete spatial and temporal information about the main plasma impurities. In order to overcome this problem, simultaneous measurements were obtained with two x-ray arrays that have markedly different spectral responses to Alcator's main light [carbon (C)] and heavy [molybdenum (Mo)] impurities. [Work directed towards a similar goal is also ongoing elsewhere.[6]] The results reported here describe the first measured impurity profiles to be quantitatively compared to the equilibrium predictions of neoclassical theory. In addition, we have observed an unambiguous connection between impurity profiles and sawtooth dynamics. This occurs through the effects impurity profiles have upon the plasma resistivity.

Figure 1a depicts the spectral efficiencies of the two x-ray arrays, A and B. Both are absolutely calibrated and conveniently cross-calibrated in-situ by operating with the same filter (A).[7] The arrays view the plasma from the same toroidal position, array A (B) from the side (bottom). For array B, with relevant Alcator conditions, only $\sim 2\%$ of the detected x rays are from Mo ions (mainly from Δn=2 transitions). This is because the filter response "cuts off" the dominant Δn=1 transitions that occur around 2.5 keV.[8]

The starting point for our analysis involves solving two equations for the C and Mo densities (n_C and n_M, respectively):

$$\frac{\epsilon^A}{n_e} - (P_H^A)n_H \simeq (P_C^A)n_C - (P_M^A)n_M \ ; \tag{1}$$

$$\frac{\epsilon^B}{n_e} - (P_H^B)n_H \simeq (P_C^B)n_C \ . \tag{2}$$

In these equations ϵ^A and ϵ^B are the absolute x-ray emissivities determined from Abel inversion; n_e is the electron density; $n_H = n_e - Z_C n_C - Z_M n_M$ [Z_C=6, $Z_M \approx 30$, and

$Z_M n_M$ is negligible]; and the P_j^k's are spectral power functions for each species j, where j stands for either H, C, or Mo, and k = filter A or B. Figure 1b depicts array-B power functions for fully-stripped H and C ions (Gaunt corrected).[9] The power functions for Mo include collisional and dielectronic excitations (large contributions),[10] and bremsstrahlung and radiative recombination (small contributions). Appropriately weighted sums are taken over the central Mo ions, +28 thru +32.[11,10] Important to our analysis is the fact that the Mo power functions have a weak dependence on the precise weighting of these ions.

Time traces of several adjacent x-ray detectors are shown in Fig. 2 for a discharge with I_p=520 kA and B_t=9.7 T (major and minor radii of 64 cm and 16.5 cm). As the pellet enters the plasma, the signals drop as $T_e(0)$ plummets from 1.6 keV to 0.6 keV. During the next 37 ms, T_e recovers and the C profile inside 7 cm gradually evolves from a "flattish" pre-pellet profile to a highly peaked one. The profile then abruptly "flattens" at the giant impurity disruption (henceforth abbreviated as G.I.D.), and thereafter carbon does not dramatically repeak. Note that from pellet injection until the G.I.D., the carbon profile is modulated by sawteeth of increasing duration. Indeed, there are many discharges in which, following pellet injection, sawtoothing eventually stops altogether (without major disruptions ensuing). Figure 2c depicts array-A emissivities, determined through Abel inversion, at critical times in the discharge of Figs. 2a and 2b. It is worthwhile to stress that, contrary to "giant" internal disruptions attributed to large temperature fluctuations,[12] the G.I.D. is of a different nature (notice the small temperature drop in Fig. 3d). In fact, the temperature perturbation of the significantly smaller internal disruption following the G.I.D. (Fig. 2a), is virtually identical to that of the G.I.D.

Figures 3a and 3b show the experimentally determined C and Mo density profiles just prior to and after the G.I.D. The dashed curves are the asymptotic equilibrium profiles predicted on the basis of a rigorous multi-ion neoclassical theory.[13] In comparing experiment with theory, it is crucial to note that C is in the plateau regime (*ie.* the C collision

frequency is less than the transit frequency). Also, because of small Mo concentrations, diffusion of C is governed by its interaction with hydrogenic (H) ions. Thus the expression for the radial C flux is[13,4]

$$\Gamma_C \propto \left[\frac{n'_H}{n_H} - \frac{n'_C}{Z_C n_C} + \frac{1.5T'}{T}\right], \tag{3}$$

where T'/T is assumed to be the same for electrons and ions, and the prime indicates differentiation with respect to r. The exact source-free equilibrium solution to the continuity equation

$$\frac{\partial n_C}{\partial t} + \nabla \cdot \mathbf{\Gamma_C} = 0 \tag{4}$$

is, using Equation (3),

$$\left(\frac{n_C}{n_C(0)}\right) = \left(\frac{n_H}{n_H(0)}\right)^{Z_C} \left(\frac{T}{T(0)}\right)^{1.5Z_C}. \tag{5}$$

Equation (5) predicts that it is the temperature profile which is responsible for peaking carbon since n_H is slightly hollow due to central ion deficit effects (Fig. 3e). Because the experimental (pre-disruption) temperature profile is well represented by a Gaussian, Equation (3) can be accurately recast as

$$\Gamma_C = -Dn'_C - n_C V\left(\frac{r}{a}\right), \tag{6}$$

where a is the minor radius. D and V are not separately constant, though the ratio, D/V, is constant. The solution of Eq. (6) for $\Gamma_C = 0$ is $n_C \propto exp[-r^2/(2aD/V)]$. From the experimental data at 257.5 ms, D/V is $0.33^{-0.18}_{-0.13}$ cm. This value is to be rigorously interpreted as an upper limit since array-B data indicate that some carbon peaking continues up to the onset of the large m=1 oscillation. (For example, see the center and outer signals in Fig. 2b.) This indicates experimentally that $\partial n_C/\partial t$ is not yet completely zero.[14] Important to our considerations here is the fact that the neoclassical prediction [Eq. (5)] represents the narrowest carbon profile that can be theoretically achieved.

From the carbon peaking that occurs in the 12 msec interval preceeding the G.I.D. (see Fig. 2a), an estimate can be made of V and D inside 4 cm. Experimentally they are found to be of order 10^3 cm/s and 300 cm^2/s respectively. The corresponding theoretical values are 500 cm/s and 150 cm^2/s respectively. Thus the measured values are of the order of the neoclassical predictions. Typically most tokamaks[4], including Alcator for non-pellet discharges[15], have reported that impurity diffusivities are one to two orders of magnitude larger than the neoclassical prediction.

The dashed curve in Fig. 3b depicts the rigorous asymptotic source-free equilibrium profile for Mo, predicted by the appropriate mixed-regime theory[13] (Mo in the PS regime, C and H in the plateau). The detailed application of this theory is outlined in Appendix-I. It is concluded there that Mo peaking is largely driven by the C profile. Thus for our experimental conditions, theory yields a Taylor-like solution[16]

$$\left(\frac{n_M}{n_M(0)}\right) \approx \left(\frac{n_C}{n_C(0)}\right)^{\frac{Z_M}{Z_C}\bar{\lambda}}, \quad (0 \lesssim r \lesssim 4 \text{ cm}) \tag{7}$$

where $\bar{\lambda}$ is a well defined correction factor due to collision frequencies and mass ratios (temperature and hydrogen gradients are shown to be subdominant in shaping Mo profiles for $0 \leq r \lesssim 4$ cm). Due to the larger error in the experimental molybdenum profile, the experimental width is determined to be between a factor of 1.3 and 3.0 that of Eq. (7). From the theoretical viewpoint, however, it is crucial to carefully consider the role of the impurity-electron friction (as represented through the equation for ambipolar balance). Specifically, molybdenum is a trace impurity, i.e., $\alpha_{Mo} \equiv \frac{n_{Mo} Z_{Mo}^2}{n_H} \sim 3 \times 10^{-3} \ll \sqrt{\frac{m_e}{m_H}}$, while carbon is a major impurity, $\alpha_C \equiv \frac{n_C Z_C^2}{n_H} \sim 1 \gg \sqrt{\frac{m_e}{m_H}}$. Thus for carbon the standard neoclassical treatment, which drops the carbon-electron friction vs. the carbon-hydrogen friction, is justified, i.e.

$$\Gamma_H + Z_C \Gamma_C \simeq 0. \tag{8}$$

(Carbon-molybdenum friction is also negligible.) For the molybdenum test particles, how-

ever, the full ambipolar balance must be considered, i.e.

$$Z_{Mo}\Gamma_{Mo} = \Gamma_e - (\Gamma_H + Z_C\Gamma_C) \tag{9}$$

Experimental estimates of the right-hand side of Eq. (9) yield a small net positive (i.e. radially outward) contribution [$\Gamma_e \lesssim \frac{10^{14}}{cm^2-s}$ at ~ 4 cm], which has the effect of broadening the molybdenum equilibrium profile of Eq. (7) by a factor of 2. Thus, inclusion of the electron friction brings the theoretical prediction well within the experimental uncertainty.

Fitting and error analysis procedures are described next. Just prior to the G.I.D., impurity levels were observed to approach a minimum at about 6.5 cm, then rise outside this radius. Equations (1) and (2) were first used to estimate C and Mo profiles inside 6.5 cm. In turn these profiles were used to construct two Gaussians corresponding to n_C and n_M whose amplitudes and widths were varied until a good fit to the original data was achieved (see Fig. 4). Errors in the e-folding widths (σ_C and σ_M) were then determined by varying n_e and T_e over their uncertainties: 15% in amplitude and 20% in width for n_e; 10% in amplitude and 20% in width for T_e. From this procedure it was determined that $\sigma_C = 3.3^{+0.8}_{-0.7}$ cm, $\sigma_M = 3.5^{+0.5}_{-1.8}$ cm, and that the relative uncertainty in the on-axis ratio of C to Mo density is $\lesssim 2$ (primarily due to the larger uncertainty in n_M).

The post-G.I.D. profiles were determined by finding acceptable fits to the change in the x-ray, interferometer (n_e), electron cyclotron (T_e), and visible bremsstrahlung signals. Starting with the pre-disruption profiles, n_e, T_e, n_C and n_M were "flattened" so as to conserve particles and energy to about 1%. Figure 3 depicts the post-disruption profiles[17] (Fig. 4 the corresponding x-ray "reconstructions"), from which it can be concluded that the unambiguous effect of the G.I.D. is to reduce on-axis impurities by a factor of 3.

Finally we posit that central carbon, the dominant non-hydrogenic contributor to Z_{eff}, has directly measurable effects on the MHD dynamics associated with the sawtooth period. As carbon gradually peaks following the pellet injection, the central Spitzer con-

ductivity (calculated on the basis of the C, Mo, and T_e profiles of Fig. 3) will hollow, leading to a flattening – possibly a hollowing – of the current profile (see i of Fig. 3f and Appendix II). This will significantly reduce the m=1 tearing rate, conventionally associated with the sawtooth disruption,[18] since the growth rate scales as $q'(r_s)^2$. [q' is the derivative of the safety factor, and r_s is the radius of the $q = 1$ singular surface.] The inhibition of the tearing mode should lengthen the sawtooth period, an effect observed during the reheat phase that follows pellet injection (Fig. 2a). In addition, if the current is sufficiently flat, the safety factor should be above 1 everywhere in the plasma. Indeed this may account for the numerous discharges where sawteeth are completely suppressed following pellet injection. (Also, major disruptions do not ensue for these cases.) In this situation highly peaked impurity profiles persist even while the temperature remains peaked on-axis. It is important to stress that this sawtooth suppression is not a result of a major change in central radiative power balance since, for the discharges discussed herein, radiation plays an insignificant role in the central power balance. [See references 1 and 3 for experiments in which central radiation is significant, sawteething stops, and the plasma disrupts.] Also directly relevant to the connection between the peakedness of the carbon profile and the sawtooth period is the observation that the carbon profile does not dramatically repeak after the G.I.D. Just after the G.I.D. the conductivity peaks (ii of Fig. 3f) and, subsequently, the sawtooth period progressively shortens (by a factor of 2.5 approximately 15 ms after the G.I.D. of Fig. 2).

In summary, differently filtered x-ray arrays have been used to simultaneously measure central carbon and molybdenum profiles, Alcator's dominant light and heavy impurities, following pellet injection. The width of the carbon profile is close to the neoclassical prediction of a source-free equilibrium state. The experimental molybdenum profile, which is more uncertain, is between a factor of 1.3 and 3.0 times that of the asymptotic prediction; theory suggests, however, that the asymptotic molybdenum profile should not be

experimentally realized as long as there is a significant radial outward diffusion of electrons (which is experimentally observed). We have no proven explanation why at first the pellet affects the impurity transport in the manner described above, whereas for non-pellet discharges (with standard sawtoothing) Alcator impurity transport is anomalous.[15] However, the hypothesis has been raised that pellet injection lowers $\eta_i \equiv \frac{\partial \ln T_i}{\partial \ln n_e}$ by a factor 2, thereby stabilizing the "ion mixing mode"[19] and permitting classical ion transport to evolve. Nor is it theoretically clear why the giant impurity disruption (G.I.D.) should end, as observed, this neoclassical-like behavior, unless, for example, it can be shown that this disruption causes η_i to rise above the instability threshold again. Further, we have presented direct experimental evidence that the central peaking (flattening) of carbon lengthens (shortens) the sawtooth period – or stops the sawtooth altogether – through measured changes in the central Spitzer conductivity profile.

From these observations there arises the concern that the thermalized alpha component of an ignited fusion plasma may be strongly peaked on-axis, depending on the (retarded) sawtooth activity in pellet fueled plasmas. And conversely, with increasing central impurity peaking, the current density may flatten, thereby greatly extending the sawtooth period or even suppressing sawteeth entirely. Since this may produce intolerably good impurity confinement, our observations imply that recent suggestions to RF-stabilize the m=1 island, in order to permit sawtooth-free operation for $q(0) < 1$ and thus high ohmic heating power levels, may have to be modified to allow periodic impurity expulsion via a deliberately induced internal disruption.

Appendix I

Ia. Neoclassical Theory for Carbon

In the inner half of the Alcator C plasma about the time of the G.I.D., carbon is in the plateau regime. Since

$$\alpha_C \equiv \frac{n_C Z_C^2}{n_H} \sim 1 \gg \sqrt{\frac{m_e}{m_H}} \text{ and}$$

$$\alpha_{Mo} \equiv \frac{n_{Mo} Z_{Mo}^2}{n_H} \sim 3 \times 10^{-3} \ll \sqrt{\frac{m_e}{m_H}} ,$$

the carbon friction with the electrons and with molybdenum is negligible, and from Reference 13, Eq. (7.43), there results our Eq. (3). The "screening coefficient" multiplying the temperature gradient term is defined in Eqs. (7.47) and (7.48). The "thermodynamic forces" , $\overline{A}_{1a}$ and $\overline{A}_{2a}$, needed in Eq. (7.43) are defined in Eqs. (7.17) and (7.16), respectively.

Ib. Neoclassical Theory for Molybdenum

Molybdenum is a trace impurity in the Pfirsch-Schlüter regime. The case of such a trace impurity in a plasma containing a main impurity has been worked out in Reference 13, Eq. (6.129). Because of the large mass ratio between molybdenum and carbon, these impurities are "weakly equilibrated" parallel to the field lines. Following the notation of Reference 13 (T=Mo), the flux for the trace impurity is expressed as

$$\Gamma_T = -D_T n_T + n_T V_T, \qquad (A.1)$$

Inside 4 cm, V_T/D_T can be well approximated by including only the effects of n_C' upon the molybdenum flux, i.e.

$$\frac{V_T}{D_T} \approx -\left(\frac{L_1 + L_2}{L_{11}^{TT}}\right) \frac{Z_T}{Z_C} \frac{n_C'}{n_C} \qquad (A.2)$$

Letting $\lambda = -\left(\frac{L_1+L_2}{L_{11}^{TT}}\right)$, which is shown in Figure A.1, the $\Gamma_T = 0$ solution of (A.1) can then be found by numerical integration. If, however, $\lambda(r)$ is approximated by its mean value $\overline{\lambda}$ (for $0 \leq r \leq 4$ cm), one immediately obtains Eq. (7) of the main text. It is worthwhile to note that the dashed curve of Figure 3b includes all the terms of Eq. 6.129 (i.e. it includes the effects due to n'_H and T', as well as that due to n'_C). However, for $r \leq 4$ cm, this result differs only slightly from the Taylor-like solution,[16] i.e. Equation (7).

Appendix II

Effect of Impurity Peaking on Current Density Evolution

Experimentally the sawtooth period is observed to lengthen after the large pellet is injected and impurity peaking is taking place. The diffusion equation for the current density is

$$\frac{\partial j}{\partial t} = \frac{1}{\mu_0}\frac{1}{r}\frac{\partial}{\partial r}r\frac{\partial}{\partial r}\eta j \tag{1}$$

where for our case of interest the Spitzer resistivity η can be written as

$$\eta = \eta_0 \frac{Z_{eff}(r,t)}{\hat{T}_e^{3/2}(r,t)} \quad , \quad \hat{T}_e = \frac{T_e(r,t)}{T_e(0,t)} \tag{2}$$

(Henceforth we will drop $\frac{\eta_0}{\mu_0}$ and let $\hat{T}_e \equiv T_e$. Also, we drop the subscript on Z_{eff}. Equation (1) becomes

$$\frac{\partial j}{\partial t} = \underbrace{\frac{1}{r}\frac{\partial}{\partial r}r\eta\frac{\partial j}{\partial r}}_{\text{I}} + j\underbrace{[\frac{1}{r}\frac{\partial}{\partial r}r\frac{\partial}{\partial r}\eta]}_{\text{II}} + \underbrace{\frac{\partial j}{\partial r}\frac{\partial \eta}{\partial r}}_{\text{III}} \tag{3}$$

Term I is a standard diffusion term and can only flatten j. Term II leads to temporal growth or damping of j depending on the sign of the second derivative of the resistivity. This describes the well known thermal instability part of the sawtooth process in a clean plasma. Term III can also contribute to growth or damping depending on the sign of the gradients. To analyze this furthur in a quantitative way, take $T_e^{-3/2} = e^{r^2/r_T^2}$ and $Z = Z_0 e^{-r^2/r_Z^2}$ (as is experimentally justified inside 7 cm), where r_T and r_Z are the profile

widths of T and Z, respectively. (For our experimental conditions following the pellet, only r_Z has a significant time dependence.) Then from (2)

$$\eta = Z_0(t)\,\epsilon^{-r^2/w^2}, \quad \text{where} \quad \frac{1}{w^2} \equiv \frac{1}{r_Z^2} - \frac{1}{r_T^2} \tag{4}$$

With impurity peaking experiments, $r_Z^2 < r_T^2$ and $w^{-2} > 0$.

Without peaking, $w^2 = -r_T^2 < 0$, which is the standard case of a clean plasma. Inserting (4) in (3) yields

$$\frac{1}{Z_0(t)}\frac{\partial j}{\partial t} = \frac{1}{r}\frac{\partial}{\partial r} r\eta \frac{\partial j}{\partial r} - j\left[\frac{4\eta}{w^2}\left(1 - \frac{r^2}{w^2}\right)\right] - \frac{\partial j}{\partial r}\eta\frac{2r}{w^2} \tag{5}$$

This indicates that inside $r_0 = w(t)$ the second term now produces damping, and outside $r_0 = w(t)$, it produces growth. The third term now produces further growth where $\frac{\partial j}{\partial r}$ is negative and further damping where $\frac{\partial j}{\partial r}$ is positive. Thus hollow current density profiles can arise, thereby dramatically changing q_0. Furthermore, such profiles can have a strong stabilizing influence on the sawtooth precursor whose growth rate depends on $\frac{\partial j}{\partial r}$ at q=1, thus lengthening the sawtooth period.

Acknowledgements

Special thanks to S. Wolfe, C. Gomez, M. Foord, E. Marmar, R. Granetz and J. Rice for interferometer, electron cyclotron, visible bremsstrahlung and x-ray data. This work has been supported in part by DOE (DE-AC02-78ET51013).

References

1. R. C. Isler, W. L. Rowan, and W. L. Hodge, Phys. Rev. Lett. 55 (22) 2413 (1985).

2. G. L. Jahns, *et al.*, Nucl. Fusion 22 (8) 1049 (1982).

3. W. Engelhardt, *et al.*, IAEA-CN-37/A-5, p. 123 (1978).

4. R. C. Isler, Nucl. Fusion 24 (12) 1599 (1984); Eq. (43) for C in the plateau regime; approximately Eq. (42) for C if in the Pfirsch-Schlüter regime; references therein.

5. D. F. Düchs and D. Pfirsch, Pl. Phys. and Cont. Nucl. Fus. Res. (Tokyo) 1, 669 (1974); D. J. Sigmar, *et al.*, ibid, 595.

6. K. Ida, R. Fonck, R. Hulse, and B. LeBlanc, PPPL #2264 (1985).

7. R. D. Petrasso, *et al.*, Rev. Sci. Instrum. 51 (5) 585 (1980); Phys. Rev. Lett. 49 (25) 1826 (1982).

8. The intrinsic power ratio of $\Delta n=2$ to $\Delta n=1$ transitions is very small, approximately 1/12 at 1.6 keV. J. Rice, private comm., 1985.

9. W. J. Karzas and R. Latter, Astrophys. J., Suppl. Ser. 6, 167 (1961).

10. E. Källne, J. Källne, and R. D. Cowan, Phys. Rev. A 27 (5) 2682 (1983).

11. C. Breton, *et al.*, Association Euratom-C.E.A. #Eur-CEA-FC-948 (1978).

12. W. Pfeiffer, *et al.*, Nucl. Fusion 25 (6) 655 (1985).

13. S. P. Hirshman and D. J. Sigmar, Nucl. Fusion 21 (9) 1079 (1981); Eq. (6.129) for Mo; Eqs. (7.43)-(7.48) for C in the plateau regime; Eq. (6.75) for C if in the Pfirsch-Schlüter regime; references therein.

14. Close analysis of array-B signals reveals that ~75% of the signal change just prior to 257.5 ms (i.e. within 1 msec) is due to the increase in temperature, with only ~25% of the change due to additional carbon peaking.

15. E. Marmar, J. Rice, J. Terry, F. Seguin, Nucl. Fusion 22 (12) 1567 (1982).

16. J. B. Taylor Nucl. Fus. Supp. 403 (1974).

17. Spectroscopic measurements of large Mo^{+30} and Mo^{+31} density fluctuations were also obtained in response to the G.I.D.

18. B. V. Waddell, G. L. Jahns, J. D. Callen, H. R. Hicks, Nucl. Fusion 18 (5) 735 (1978); G. Bateman, *MHD Instabilities*, MIT Press, p. 221 (1978); references therein.

19. J. W. Connor, Nuclear Fusion 26 193 (1986); references therein.

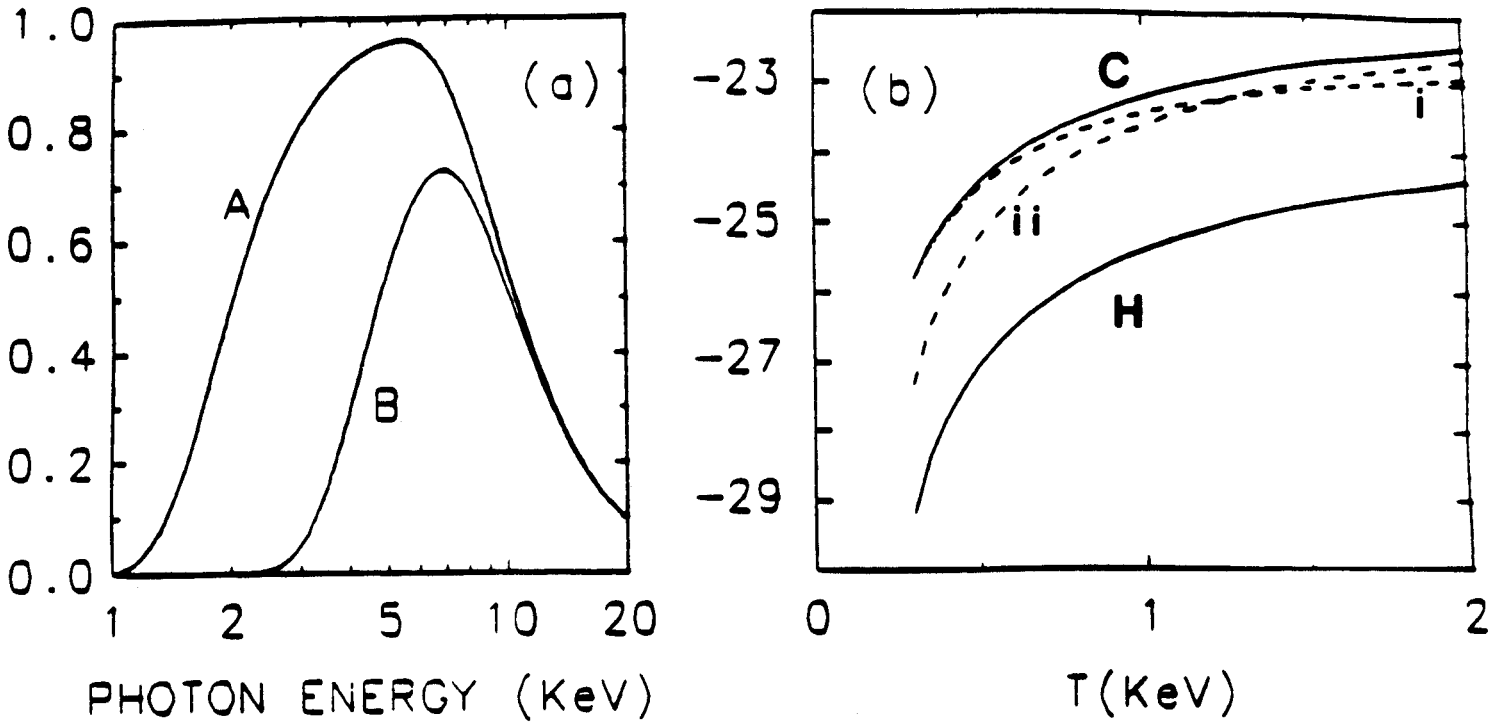

Fig. 1 (a) X-ray spectral efficiencies for arrays A and B. The low-energy response results from 10.0 mg/cm^2 Be for A; and from 10.0 mg/cm^2 Be plus 30.4 mg/cm^2 C for B. The high-energy response results from the finite detector thickness (23.3 mg/cm^2 Si). (b) Array-B power functions for the hydrogen (H) and carbon (C) x-ray continua. Recombination (i) and bremsstrahlung (ii) components of carbon are individually depicted, the former dominating for $T_e < 1.3$ keV [units of erg-cm^3/s; vertical scale in $\log_{10}$]. All calculations of the continua include appropriate Gaunt corrections.[9]

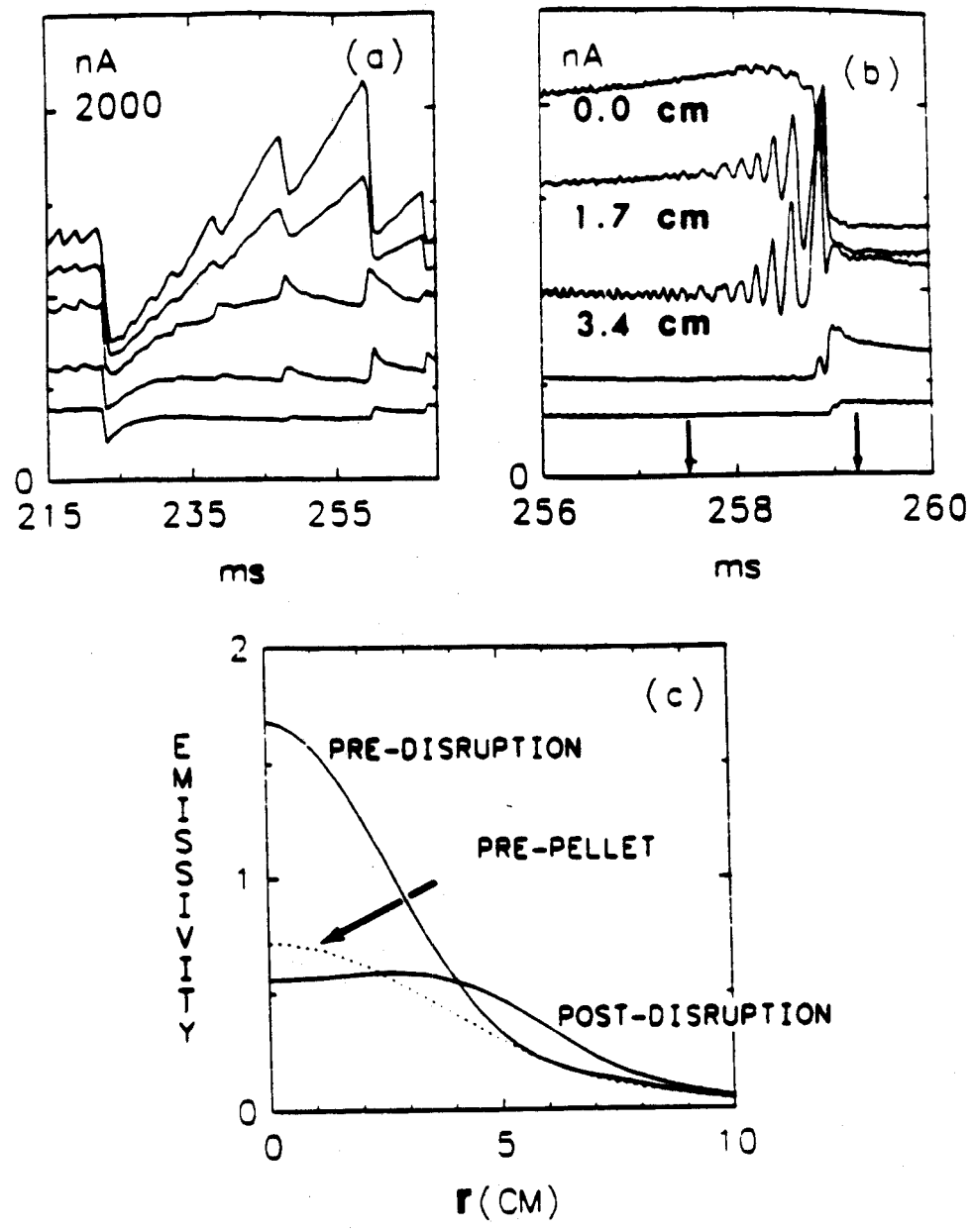

Fig. 2 (a) Several x-ray signals for adjacent array-A detectors viewing chords separated by 1.7 cm (shot # 25). The top signal corresponds to the center-viewing detector. The pellet enters the plasma at about 223 ms; the giant impurity disruption (G.I.D.) occurs at about 259 ms [units of nano-amps (nA)]. (b) Same as (a), but time-expanded about the G.I.D; the arrows indicate times of analysis for all subsequent figures. (c) Absolute array-A x-ray emissivities just before the pellet (dashed line), and just before (257.5 ms) and after (259.3 ms) the G.I.D. (solid lines) [units of 10^6 erg/(cm^3-s)].

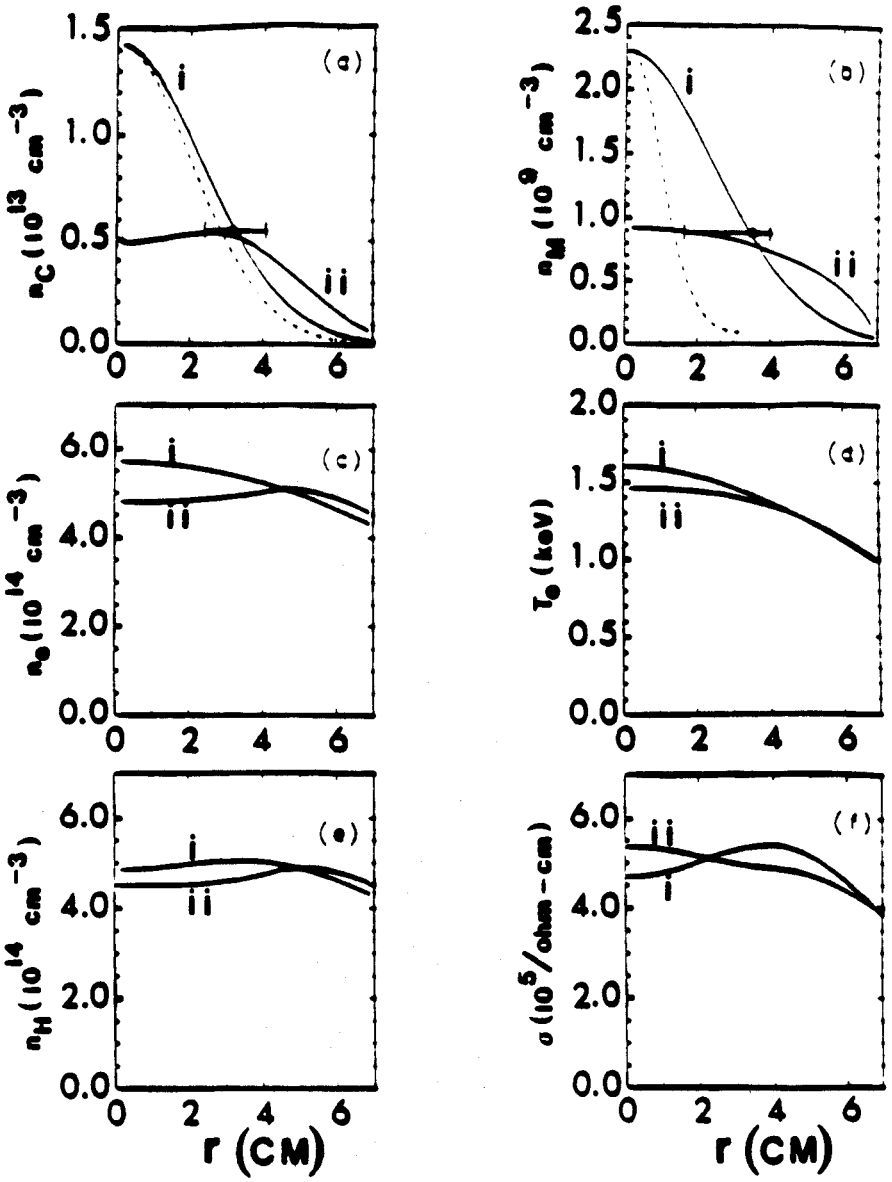

Fig. 3 (a) Experimental carbon density profiles just before (i) and just after (ii) the giant impurity disruption (G.I.D.), at the times indicated in Fig. 2b [units of 10^{13} cm $^{-3}$]. Outside of $\sim$ 6.5 cm, the impurity concentrations increase. The dashed curve is the asymptotic equilibrium prediction. (b) Same as for (a), but for molybdenum [units of 10^9 cm^{-3}]. (c) Corresponding n_e profiles [units of 10^{14} cm^{-3}]. (d) Corresponding T_e profiles [units of keV]. (e) Corresponding n_H profiles [units of 10^{14} cm^{-3}]. (f) Corresponding Spitzer conductivity profiles [units of 10^5 (ohm-cm)$^{-1}$]. The *relative* error in the conductivity profile is $\lesssim$5%, the absolute error $\lesssim$15%.

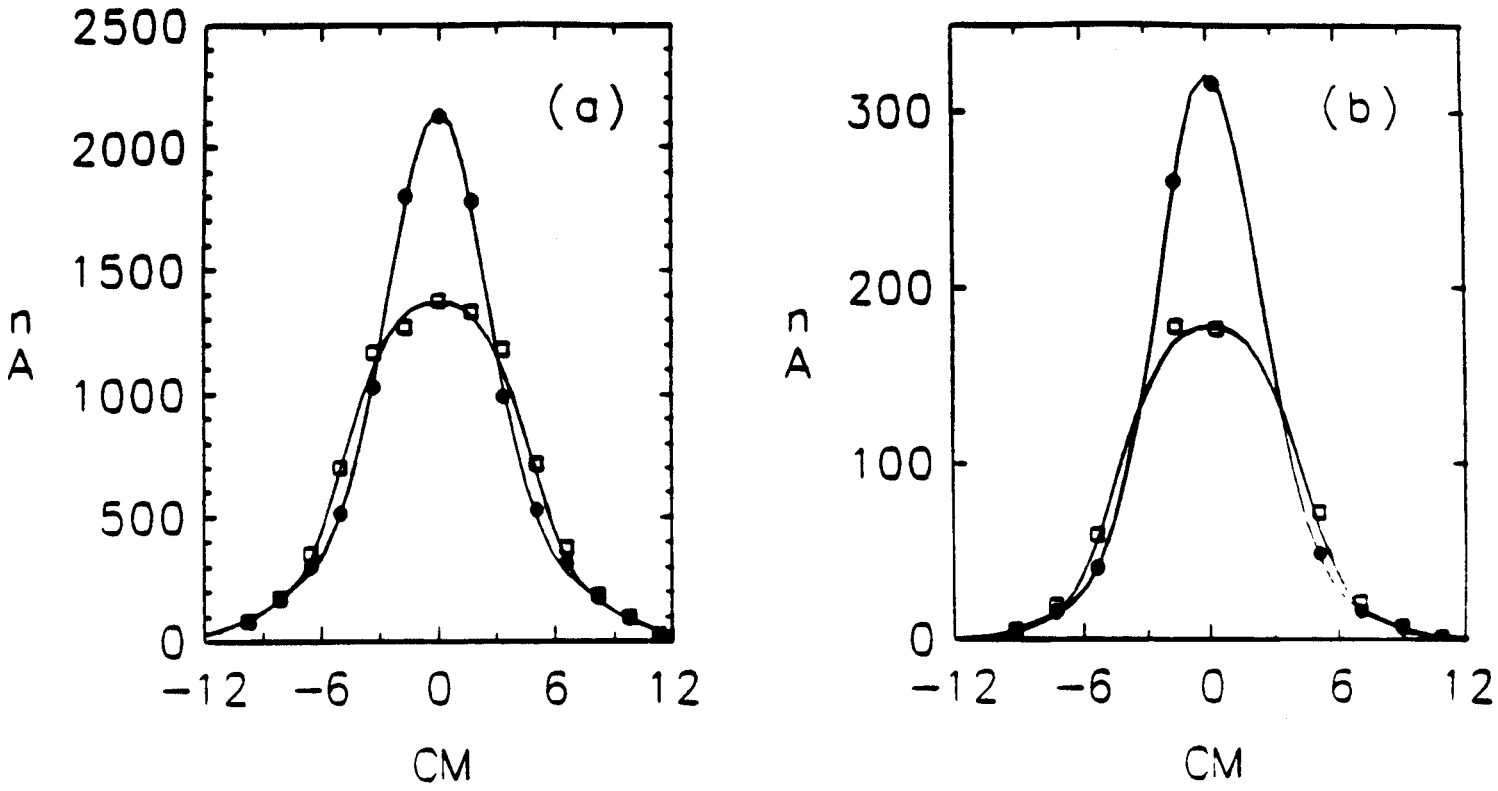

Fig. 4 (a) Array-A pre (•) and post (□) x-ray "brightness" data just before and just after the giant impurity disruption (G.I.D.) of Fig. 2. The lines are from "reconstructing" models of the x-emission, as described in the text [units of nano-amps (nA)]. (b) Same as (a), but for array B. [The relative error in all x-ray data points is $\lesssim$5%; the absolute error of the entire data set (A&B) is $\lesssim$10%. The noise level of each data point, ~0.5 nA,[7] is significantly smaller than the signals.]

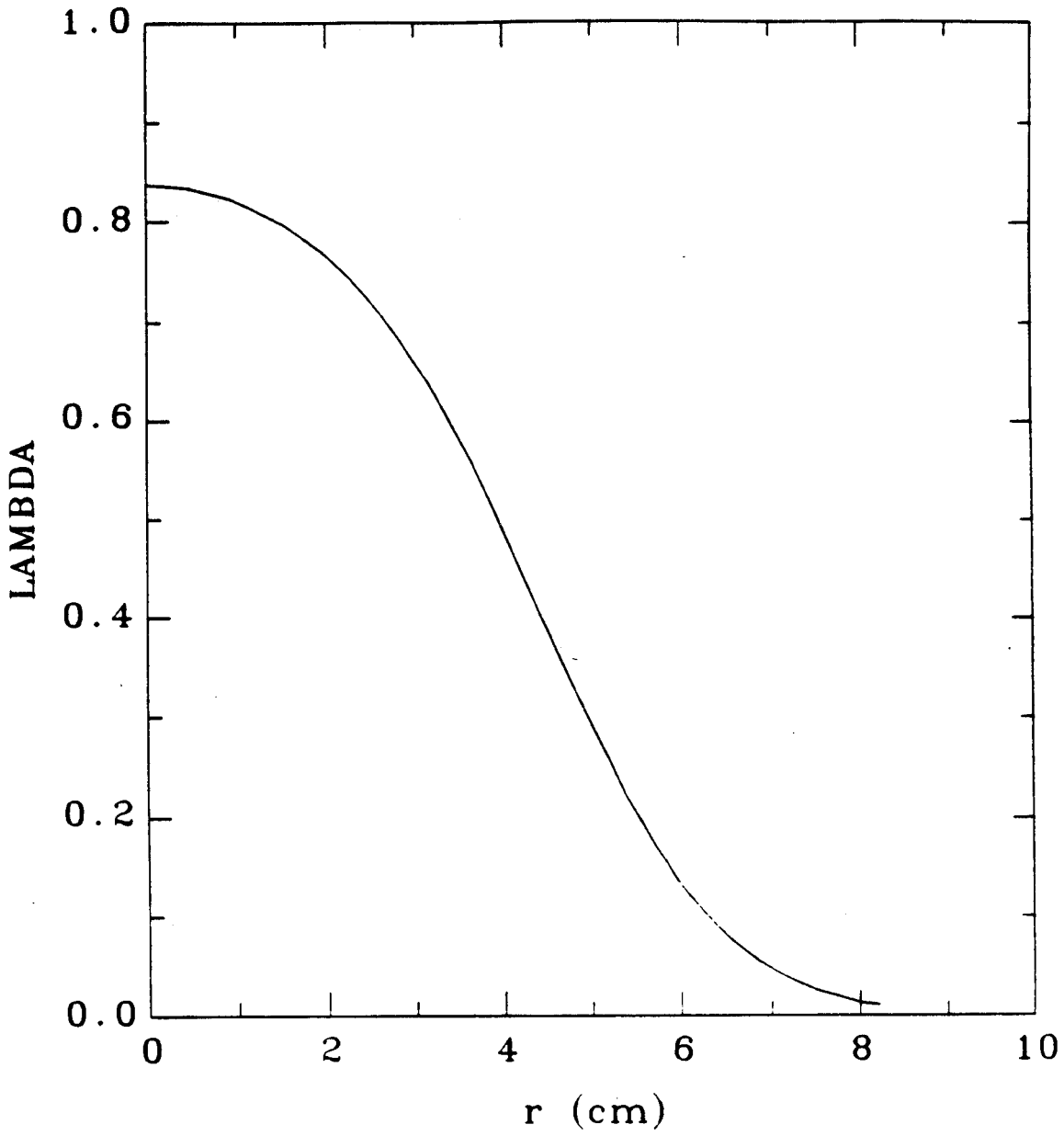

Fig. A1. The function λ, used in obtaining the Taylor-like solution (Equation 7) for the molybdenum asymptotic profile. In Equation (7), $\bar{\lambda}$ is the mean value between 0 and 4 cm.

Appendix II

Effect of Impurity Peaking on Current Density Evolution

Experimentally the sawtooth period is observed to lengthen after the large pellet is injected and impurity peaking is taking place. The diffusion equation for the current density is

$$\frac{\partial j}{\partial t} = \frac{1}{\mu_0}\frac{1}{r}\frac{\partial}{\partial r} r \frac{\partial}{\partial r}\eta j \tag{1}$$

where for our case of interest the Spitzer resistivity η can be written as

$$\eta = \eta_0 \frac{Z_{eff}(r,t)}{\hat{T}_e^{3/2}(r,t)} \quad , \quad \hat{T}_e = \frac{T_e(r,t)}{T_e(0,t)} \tag{2}$$

(Henceforth we will drop $\frac{\eta_0}{\mu_0}$ and let $\hat{T}_e \equiv T_e$. Also, we drop the subscript on Z_{eff}. Equation (1) becomes

$$\frac{\partial j}{\partial t} = \underbrace{\frac{1}{r}\frac{\partial}{\partial r} r\eta \frac{\partial j}{\partial r}}_{\text{I}} + j\underbrace{\left[\frac{1}{r}\frac{\partial}{\partial r} r \frac{\partial}{\partial r}\eta\right]}_{\text{II}} + \underbrace{\frac{\partial j}{\partial r}\frac{\partial \eta}{\partial r}}_{\text{III}} \tag{3}$$

Term I is a standard diffusion term and can only flatten j. Term II leads to temporal growth or damping of j depending on the sign of the second derivative of the resistivity. This describes the well known thermal instability part of the sawtooth process in a clean plasma. Term III can also contribute to growth or damping depending on the sign of the gradients. To analyze this furthur in a quantitative way, take $T_e^{-3/2} = e^{r^2/r_T^2}$ and $Z = Z_0 e^{-r^2/r_Z^2}$ (as is experimentally justified inside 7 cm), where r_T and r_Z are the profile

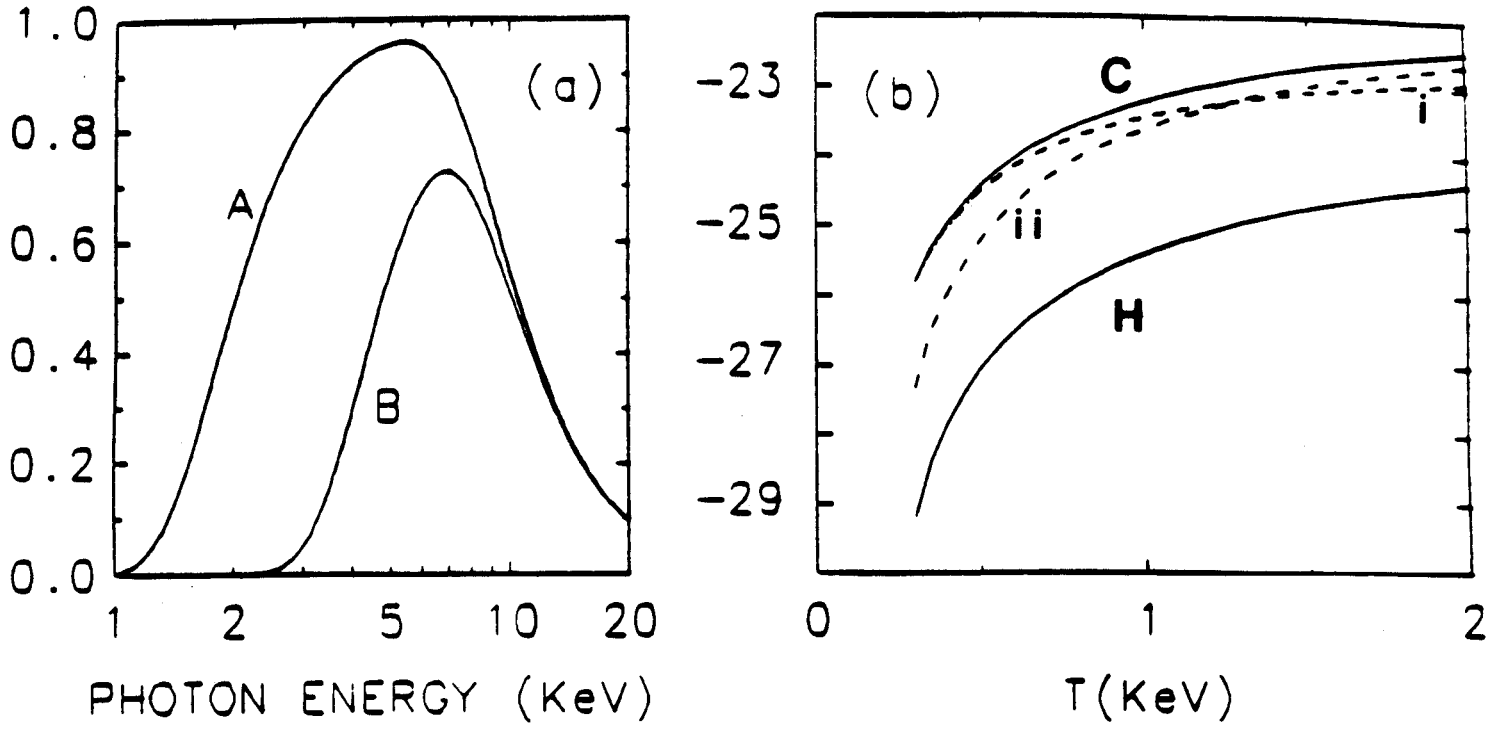

Fig. 1 (a) X-ray spectral efficiencies for arrays A and B. The low-energy response results from 10.0 mg/cm^2 Be for A; and from 10.0 mg/cm^2 Be plus 30.4 mg/cm^2 C for B. The high-energy response results from the finite detector thickness (23.3 mg/cm^2 Si). (b) Array-B power functions for the hydrogen (H) and carbon (C) x-ray continua. Recombination (i) and bremsstrahlung (ii) components of carbon are individually depicted, the former dominating for $T_e < 1.3$ keV [units of erg-cm^3/s; vertical scale in $\log_{10}$]. All calculations of the continua include appropriate Gaunt corrections.[9]

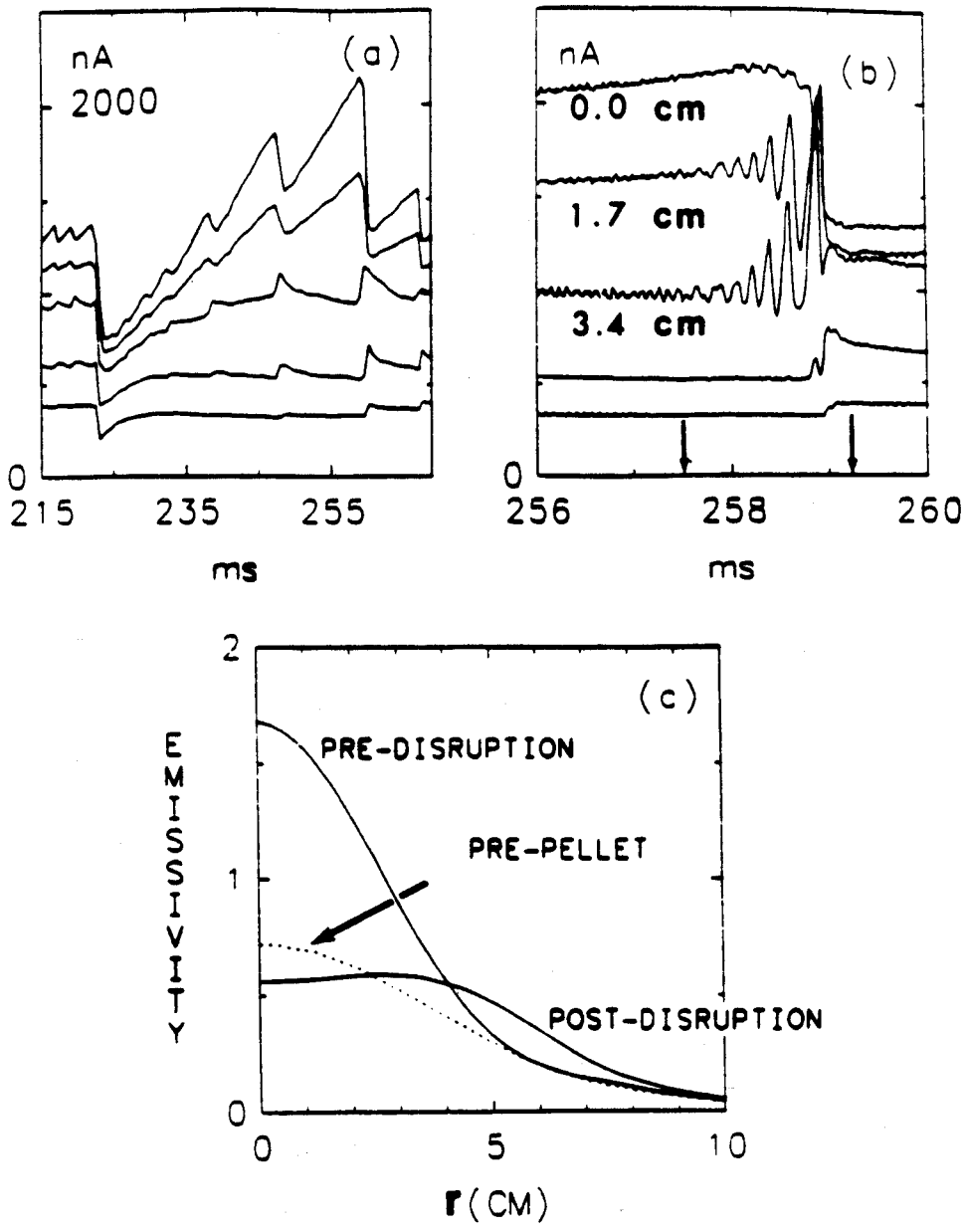

Fig. 2 (a) Several x-ray signals for adjacent array-A detectors viewing chords separated by 1.7 cm (shot # 25). The top signal corresponds to the center-viewing detector. The pellet enters the plasma at about 223 ms; the giant impurity disruption (G.I.D.) occurs at about 259 ms [units of nano-amps (nA)]. (b) Same as (a), but time-expanded about the G.I.D; the arrows indicate times of analysis for all subsequent figures. (c) Absolute array-A x-ray emissivities just before the pellet (dashed line), and just before (257.5 ms) and after (259.3 ms) the G.I.D. (solid lines) [units of 10^6 erg/(cm^3-s)].

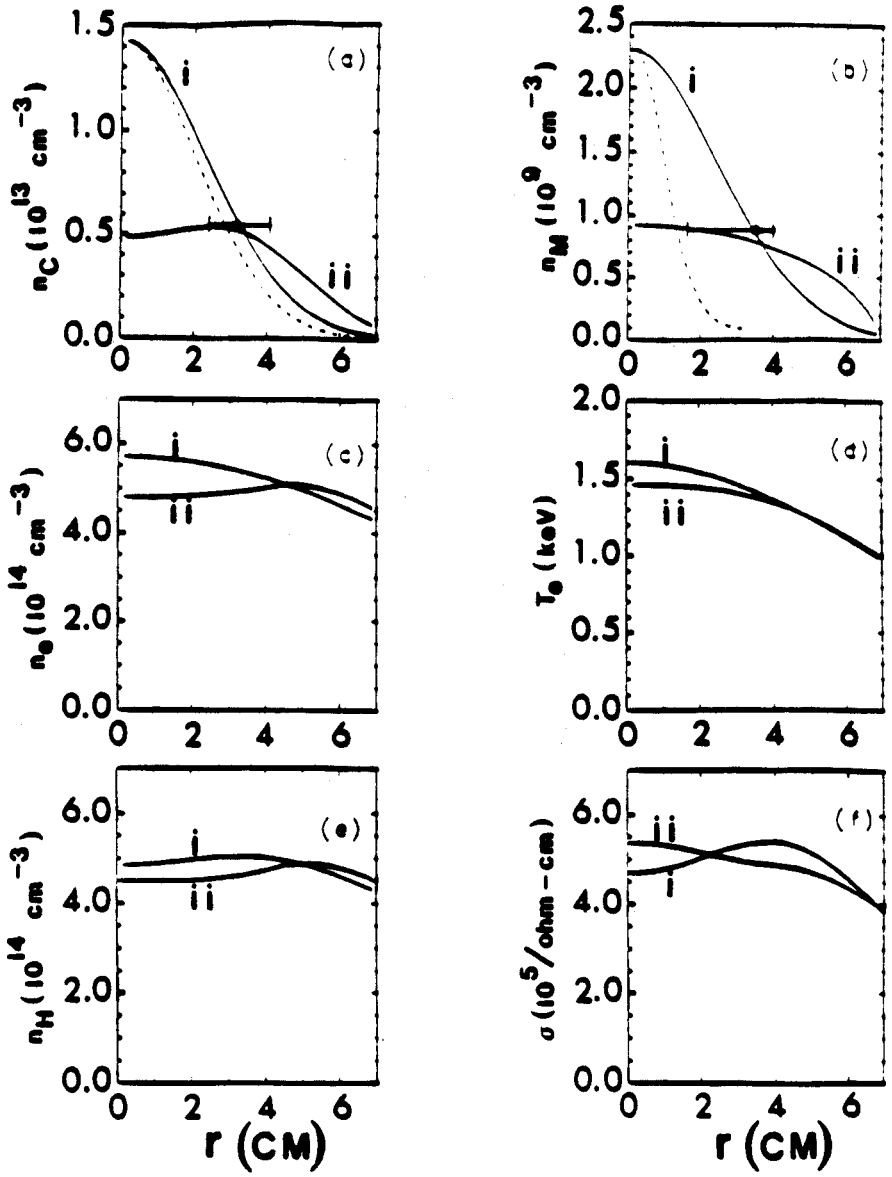

Fig. 3 (a) Experimental carbon density profiles just before (i) and just after (ii) the giant impurity disruption (G.I.D.), at the times indicated in Fig. 2b [units of 10^{13} cm^{-3}]. Outside of $\sim$ 6.5 cm, the impurity concentrations increase. The dashed curve is the asymptotic equilibrium prediction. (b) Same as for (a), but for molybdenum [units of 10^{9} cm^{-3}]. (c) Corresponding n_e profiles [units of 10^{14} cm^{-3}]. (d) Corresponding T_e profiles [units of keV]. (e) Corresponding n_H profiles [units of 10^{14} cm^{-3}]. (f) Corresponding Spitzer conductivity profiles [units of 10^{5} (ohm-cm)$^{-1}$]. The *relative* error in the conductivity profile is $\lesssim$5%, the absolute error $\lesssim$15%.

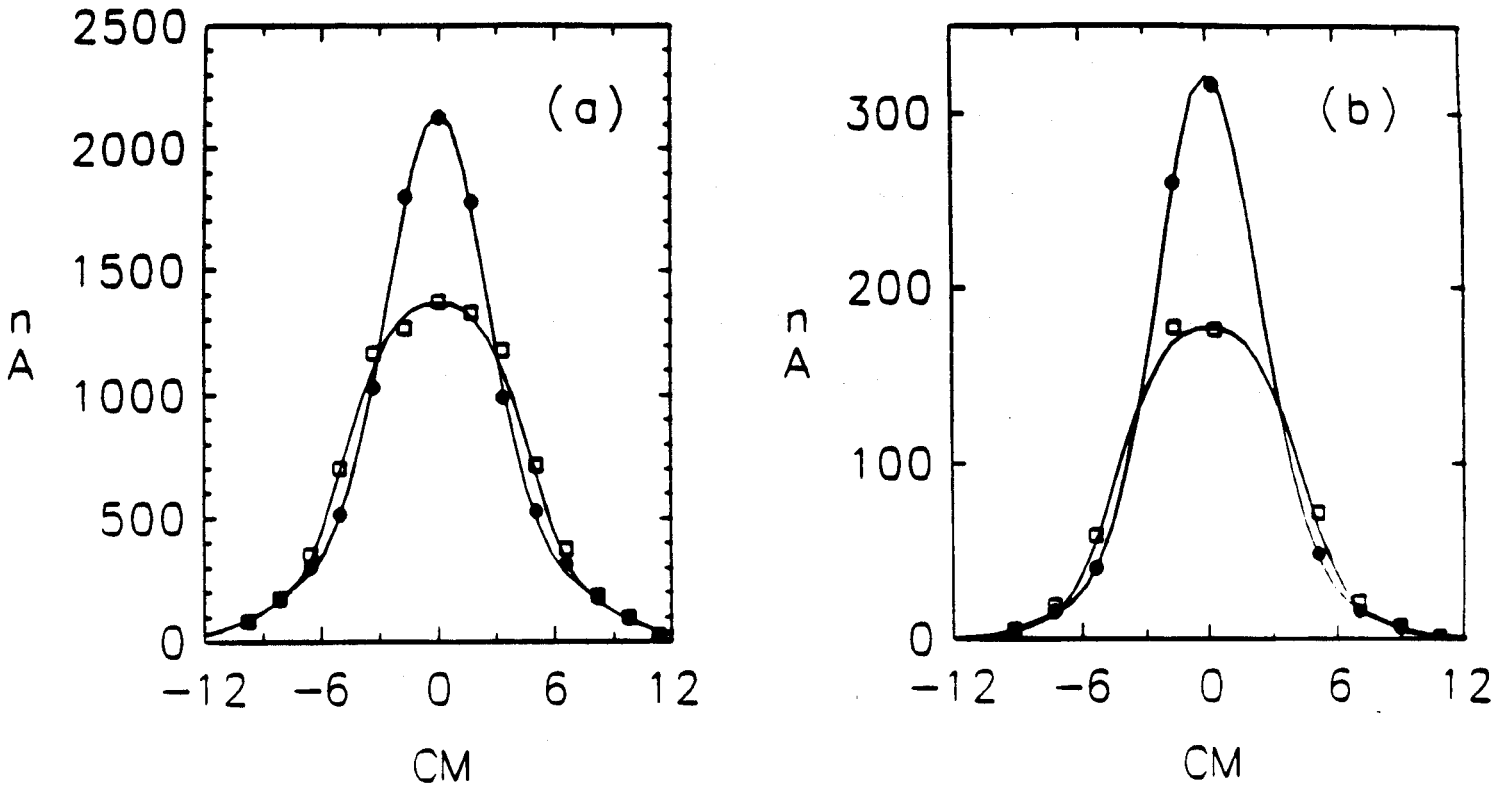

Fig. 4 (a) Array-A pre (•) and post (□) x-ray "brightness" data just before and just after the giant impurity disruption (G.I.D.) of Fig. 2. The lines are from "reconstructing" models of the x-emission, as described in the text [units of nano-amps (nA)]. (b) Same as (a), but for array B. [The relative error in all x-ray data points is $\lesssim$5%; the absolute error of the entire data set (A&B) is $\lesssim$10%. The noise level of each data point, ~0.5 nA,[7] is significantly smaller than the signals.]

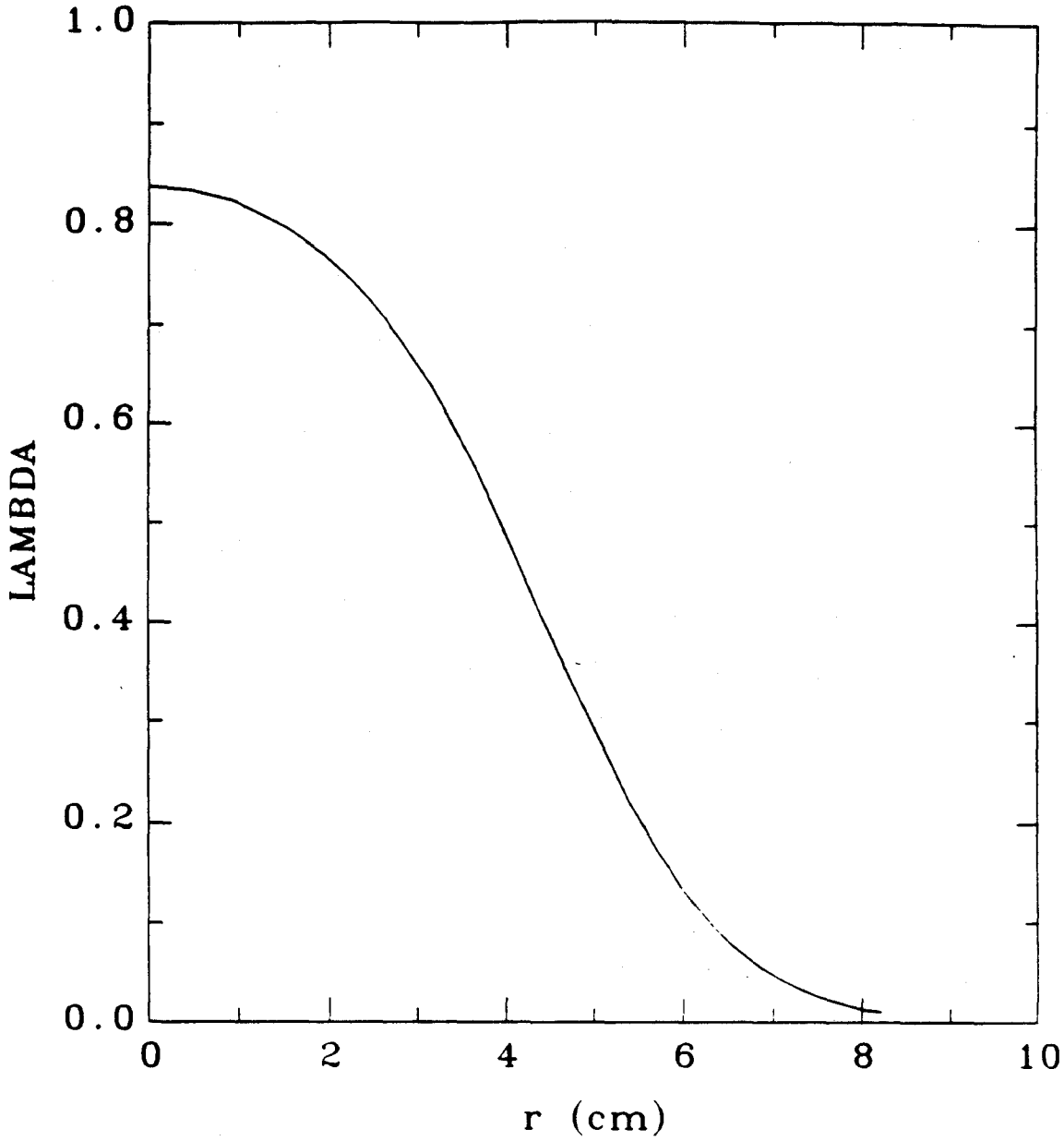

Fig. A1. The function λ, used in obtaining the Taylor-like solution (Equation 7) for the molybdenum asymptotic profile. In Equation (7), $\bar{\lambda}$ is the mean value between 0 and 4 cm.

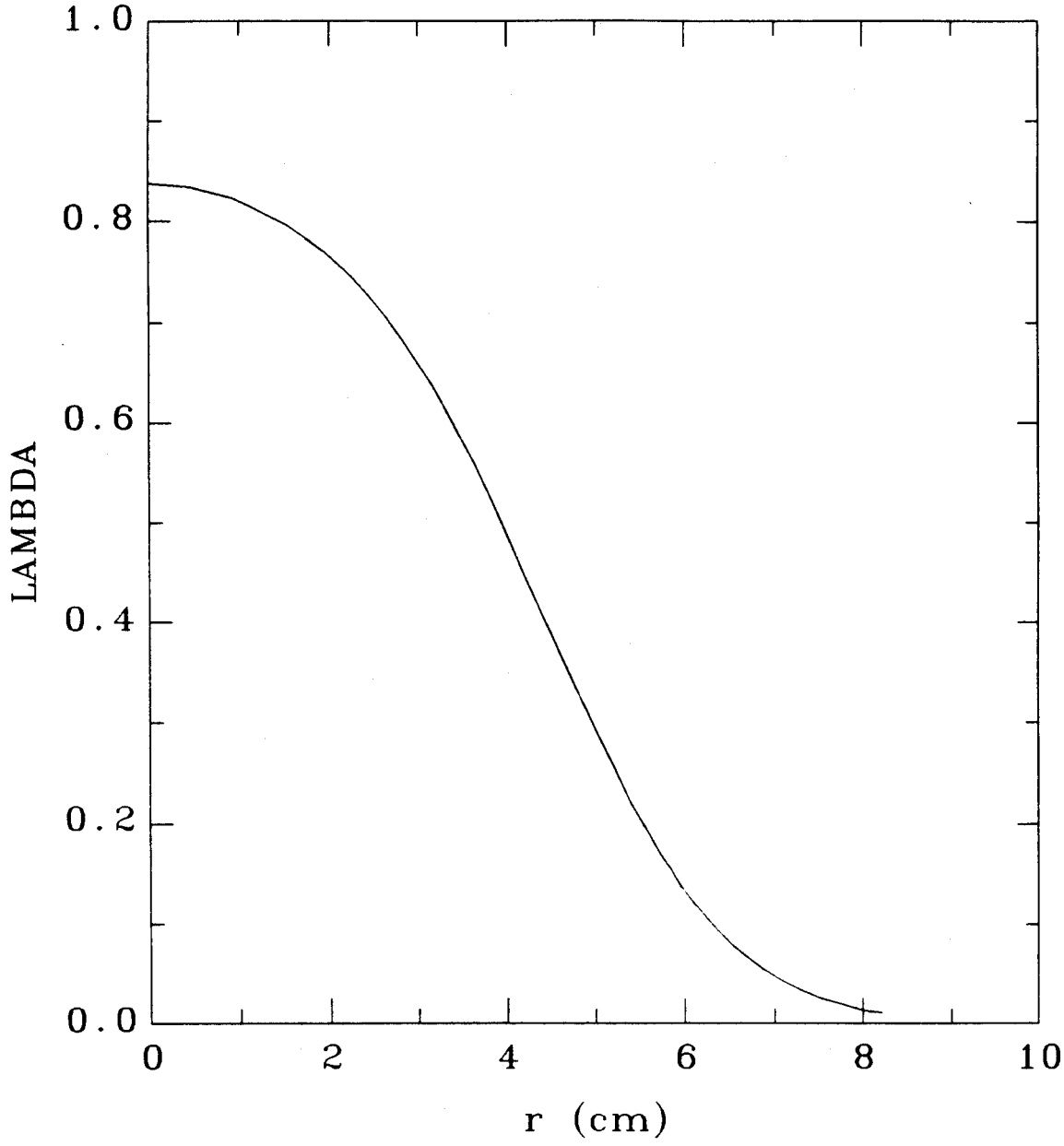
1.0
0.8
0.6
0.4
0.2
0.0
LAMBDA
0
2
4
6
8
10
r (cm)